Earth and Planetary Science Letters 530 (2020) 115923

Contents lists available at ScienceDirect

Earth and Planetary Science Letters

www.elsevier.com/locate/epsl

Core formation and geophysical properties of Mars

Matthew C. Brennan [a,*], Rebecca A. Fischer [a], Jessica C.E. Irving [b]

[a] Harvard University, Department of Earth and Planetary Sciences, United States of America
[b] Princeton University, Department of Geosciences, United States of America

ARTICLE INFO

Article history:
Received 1 February 2019
Received in revised form 10 October 2019
Accepted 21 October 2019
Available online 11 November 2019
Editor: J. Brodholt

Keywords:
Mars
core formation
Fe–S alloys
Martian core
InSight

ABSTRACT

The chemical and physical properties of the interiors of terrestrial planets are largely determined during their formation and differentiation. Modeling a planet's formation provides important insights into the properties of its core and mantle, and conversely, knowledge of those properties may constrain formational narratives. Here, we present a multi-stage model of Martian core formation in which we calculate core–mantle equilibration using parameterizations from high pressure–temperature metal–silicate partitioning experiments. We account for changing core–mantle boundary (CMB) conditions, composition-dependent partitioning, and partial equilibration of metal and silicate, and we evolve oxygen fugacity (fO_2) self-consistently. The model successfully reproduces published meteorite-based estimates of most elemental abundances in the bulk silicate Mars, which can be used to estimate core formation conditions and core composition. This composition implies that the primordial material that formed Mars was significantly more oxidized (0.9–1.4 log units below the iron–wüstite buffer) than that of the Earth, and that core–mantle equilibration in Mars occurred at 42–60% of the evolving CMB pressure. On average, at least 84% of accreted metal and at least 40% of the mantle were equilibrated in each impact, a significantly higher degree of metal equilibration than previously reported for the Earth. In agreement with previous studies, the modeled Martian core is rich in sulfur (18–19 wt%), with less than one weight percent O and negligible Si.

We have used these core and mantle compositions to produce physical models of the present-day Martian interior and evaluate the sensitivity of core radius to crustal thickness, mantle temperature, core composition, core temperature, and density of the core alloy. Trade-offs in how these properties affect observable physical parameters like planetary mass, radius, moment of inertia, and tidal Love number k_2 define a range of likely core radii: 1620–1870 km. Seismic velocity profiles for several combinations of model parameters have been used to predict seismic body-wave travel times and planetary normal mode frequencies. These results may be compared to forthcoming Martian seismic data to further constrain core formation conditions and geophysical properties.

1. Introduction

At present, most of our knowledge of the Martian interior relies on inferences from meteorites and measurable geophysical properties, such as planetary mass, inertia, and tidal responses. While the ongoing InSight mission may directly measure the seismic properties of the interior (Panning et al., 2017), interpreting these data will require an understanding of the Martian composition.

Martian mantle composition can be determined by extrapolating the compositions of Martian meteorites, particularly the Shergotty-Nakhla-Chassigny (SNC) group, back to their source. Dreibus and Wänke (1985) developed the canonical model for the silicate Mars (updated by Taylor, 2013) by measuring SNC elemental abundances and proposing that their ratios reflect a mixture of volatile-rich and volatile-poor materials. In later studies, such as Lodders and Fegley (1997) and Sanloup et al. (1999), compositional models were constructed by matching the oxygen isotopic composition of the SNCs to mixtures of chondrites. From these studies, Mars is interpreted to have an FeO-enriched mantle and a smaller core mass fraction relative to Earth, indicating more oxidizing formational conditions (e.g., Rubie et al., 2011). The proximity of Mars to the protoplanetary snow line during its formation may have resulted in accretion of a larger portion of relatively oxidized, volatile-rich material. Mars is also thought to have a sulfur-rich core based on mass balance arguments (e.g., Anderson, 1972) and chalcophile element depletions (e.g., Wänke, 1991; Wänke and Dreibus, 1988; Yang et al., 2015). Sulfur-rich iron alloys have low

* Corresponding author at: 20 Oxford St, Cambridge, MA, 02138, United States of America.
E-mail address: mcbrennan@g.harvard.edu (M.C. Brennan).

https://doi.org/10.1016/j.epsl.2019.115923
0012-821X/

melting temperatures, so a high S content may have prevented crystallization of an inner core, consistent with the lack of a modern Martian geodynamo (Helffrich, 2017; Williams and Nimmo, 2004).

One difficulty in evaluating compositional models is determining whether they accurately reflect the behavior of materials during core formation. Single-stage differentiation models use metal–silicate partitioning data to determine one pressure–temperature–oxygen fugacity (P–T–fO_2) condition that can simultaneously reproduce the abundances of several elements (e.g., Rai and van Westrenen, 2013; Righter and Chabot, 2011; Steenstra and van Westrenen, 2018). However, these models do not account for changing conditions during planetary growth, so it is important to check such conclusions with more realistic models. Multi-stage core formation models can constrain the conditions of core formation by comparing the meteorite-based mantle elemental abundances to those calculated at different model conditions for the subset of elements sensitive to the style of core formation (e.g., depth evolution and degree of equilibration). Rubie et al. (2015) calculated Martian core formation in a multi-stage model with self-consistent fO_2 evolution, though their model did not include S and only used the Martian FeO content as a constraint.

Core formation has implications for the modern-day physical state of the Martian interior. Previous studies developed models of the Martian interior that match geophysical parameters such as bulk density and moment of inertia factor (MOI) and geochemical properties inferred from SNC meteorites (e.g., Bertka and Fei, 1998; Khan et al., 2018; Nimmo and Faul, 2013; Plesa et al., 2018; Rivoldini et al., 2011; Sohl and Spohn, 1997). Sohl and Spohn (1997) developed one model that matched the MOI and another that matched the Fe/Si ratio of Mars. These models improved on earlier assessments by using equations of state to calculate the behavior of Martian minerals at high P–T and constrained the core size to 1400–1700 km. Bertka and Fei (1998) found a core size compatible with this range for Fe–14 wt% S (~1400 km). Later measurements of the MOI of Mars, its tidal Love number (k_2), and its tidal dissipation factor (Q) seemed to only be matched by models with larger cores. For example, Rivoldini et al. (2011) found that MOI and k_2 were best matched by cores 1730–1860 km in radius. Varying parameters such as core density and mantle thermal structure can produce models that match these same constraints at a range of core sizes (Nimmo and Faul, 2013), so it is important to evaluate the influence of these parameters. Khan et al. (2018) inverted for the most likely ranges of several properties, including core composition, CMB temperature, and lithospheric thickness, and they constructed seismic velocity profiles based on these ranges. These results suggest a large core (1730–1840 km), though their Bayesian method does not explicitly consider the influence of each parameter on the determined core size. Plesa et al. (2018) also found that the core must be large (>1800 km) based on thermal evolution modeling. Larger cores have lower CMB pressures, probably precluding a bridgmanite layer, though Bertka and Fei (1997) determined that the existence of Martian bridgmanite is also highly temperature dependent.

Here we present a new model of Martian core formation, which improves upon previous studies by implementing multi-stage differentiation with comparisons to a large suite of major, minor, and trace elements. The core and mantle compositions predicted by this core formation model were used to construct forward models of modal mineralogy, density, and seismic velocity profiles for the Martian interior. We explicitly considered how planetary structure is influenced by core composition as well as geophysical parameters such as crustal thickness and thermal structure. Additionally, we introduced more realistic estimations of liquid Fe–S alloy densities at high P–T, improving our understanding of the core's physical properties. Assessing seismic properties across the model suite allowed for predictions of both body wave travel times and normal mode oscillation frequencies. These new self-consistent models of core formation, internal structure, and seismic properties help tie together the formation of Mars with its modern state and produce geophysical predictions that can be compared to seismic results obtained by the InSight mission.

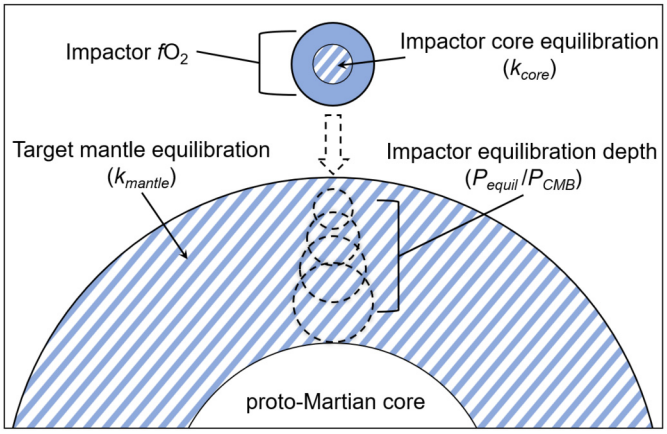

Fig. 1. Schematic of a small body (the impactor) accreting to proto-Mars (the target) in the core formation model. Solid shaded regions equilibrate fully, unshaded ones do not equilibrate, and stripes denote partial equilibration. In this homogenous accretion scenario, the values of the parameters represent effective averages over the conditions of Martian core formation.

2. Methods

We have constructed a model of multi-stage core formation to investigate Martian formational properties and a model of planetary physical structure to investigate geophysical properties of modern Mars. Further details on these, as well as our seismological calculations, can be found in the supplementary materials.

2.1. Core formation

Chondritic primordial material was equilibrated at a single fO_2 to form planetesimals, which were sequentially added to the proto-Mars, and experimentally-determined metal–silicate partitioning data (Supplementary Table S1) were used to model the chemistry of core formation (e.g., Fischer et al., 2017; Rubie et al., 2011; 2015). In order to constrain the core formation conditions required to match the previously-published SNC-based Martian mantle composition, we used the same bulk planetary composition that Taylor (2013) proposed to explain the Martian mantle. This bulk composition was based on CI chondrites enriched in refectory elements (Mg, Al, Si, Ca, V, Cr, Fe, Co, Ni, W, Ti) by a factor of 1.9 to create relative depletions in more volatile elements (Na, P, S, K, Mn). Dynamical studies suggest that Mars likely did not experience giant impacts (e.g., O'Brien et al., 2014), so we constructed Mars from 1000 small impactors. The final composition of Mars is insensitive to the specific impactor quantity for large numbers of impactors.

In each accretionary step, one planetesimal (the impactor) was equilibrated with proto-Mars (the target). Following the example of previous partial-equilibration models (e.g., Rudge et al., 2010), equilibration took place between the entire impactor mantle, a portion of the impactor core, and a portion of the target mantle; the core of proto-Mars was assumed to be undisturbed by impacts (Fig. 1). In each step, metal–silicate equilibration took place at a constant fraction of the growing CMB pressure and at the liquidus temperature. Pressure at the CMB increased linearly with mass, using 21 GPa as the final CMB pressure (Rivoldini et al., 2011). Mg, Al, Ca, Na, and K were assumed to be perfectly lithophile. In each

step, major elements Si, Fe, O, and Ni were partitioned first, allowing fO_2 to evolve self-consistently following the methodology of Rubie et al. (2011) as updated in Fischer et al. (2017), then S and the trace elements were partitioned. Finally, the unequilibrated portion of the impactor core and the metallic portion of the equilibrated material were added to the proto-Martian core, and the unequilibrated portion of the target mantle and the silicate portion of the equilibrated material were combined to form the proto-Martian mantle. This procedure assumes a homogenous accretion scenario and constrains only the average conditions of Martian core formation. Nonetheless, homogenous accretion may be a good approximation if Mars is a stranded planetary embryo that accreted most of its mass oligarchically (e.g., Dauphas and Pourmand, 2011).

Adjustable parameters in the model include: the equilibration fraction (the portion that participates in the metal–silicate reaction) of the impactor core (denoted by k_{core}) and target mantle (k_{mantle}); depth of equilibration, expressed as a fraction of the evolving CMB pressure (P_{equil}/P_{CMB}); and the initial oxidation state of the impactor bodies (Fig. 1). To evaluate the sensitivity of the resulting compositions to these formational parameters and to constrain them, the equilibration fractions of the impactor core and target mantle were each varied in the range 0.1–1.0, the depth of equilibration was varied in the range 0.01–1.0, and the constant initial fO_2 of the accreted material was varied from IW–3 to IW. Temporal changes in the fO_2 of accreting material were not considered. Compositional uncertainties due to the reported experimental uncertainties of the partition coefficients were evaluated using a Monte Carlo analysis.

2.2. Physical structure

Using the core and mantle compositions calculated in the core formation model, present-day radial profiles of density and seismic wave speeds were constructed for a range of geophysical parameters. The Martian temperature profile (the "aerotherm") was calculated based on an adiabat from the median CMB conditions of Rivoldini et al. (2011) (~21 GPa and ~2000 K). These correspond to a mantle potential temperature of ~1600 K, consistent with previous estimates (e.g., Nimmo and Faul, 2013; Zheng et al., 2015). The lithospheric thermal boundary layer was approximated as a layer of linearly increasing temperature that intersects the adiabat at ~200 km, the estimated base of the thermal boundary (e.g., Khan et al., 2018). Using these temperatures, mantle profiles of modal mineralogy, rigidity, density, and seismic wave speeds were calculated using Perple_X (Connolly, 2009) with the thermophysical dataset of Stixrude and Lithgow-Bertelloni (2011).

The Martian core was assumed to be a homogenous liquid Fe–S alloy, with the S fraction specified by the core formation model. Density–pressure relationships for the core were calculated by reference to published Fe–S alloy equations of state. The core S content is a function of the formational parameters discussed above, so it was necessary to interpolate between equations of state for several alloys to calculate densities over a range of compositions. We used four equations of state: γ-Fe (Komabayashi and Fei, 2010), Fe_3S (Seagle et al., 2006), FeS (Urakawa et al., 2004), and FeS_2 (Thompson et al., 2016). These equations of state all describe solids, so we applied a correction for the difference in molar volume between these and liquid alloys using the Clapeyron equation, the Fe–S eutectic melting curve (Campbell et al., 2007), and Fe–S ambient latent heat (Mare et al., 2014). We also performed calculations holding the volume change of melting ($\Delta V_{melting}$) fixed to various values spanning the range of $\Delta V_{melting}$ between those of Fe and FeS (e.g., Anderson and Ahrens, 1994; Komabayashi and Fei, 2010; Nishida et al., 2011). While it would have been more straightforward to use liquid equations of state, there are not enough data to adequately constrain liquid Fe–S alloy densities over a range of compositions (Section 4.4).

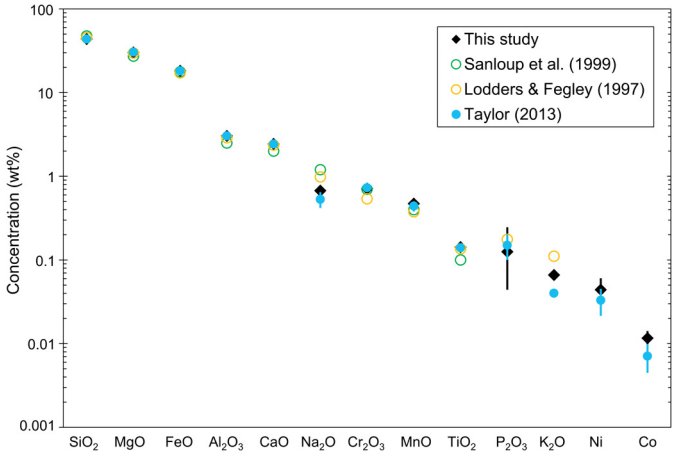

Fig. 2. Comparison of bulk mantle compositions between this study and models based on SNC elemental abundances (Taylor, 2013) or O isotopes (Lodders and Fegley, 1997; Sanloup et al., 1999). Error bars correspond to 95% confidence intervals of our Monte Carlo error analysis for this study and reported 2σ uncertainties for Taylor (2013). Calculation was performed for $k_{core} = 0.9$, whole mantle equilibration ($k_{mantle} = 1$), $P_{equil}/P_{CMB} = 0.55$, and initial fO_2 of IW–1.12.

Pressure versus density and pressure versus velocity profiles were converted to functions of depth with a thin-shell model of self-gravitation (see supplementary materials for more details). Each constructed profile corresponds to a specific set of physical (crustal thickness, mantle temperature, core temperature, $\Delta V_{melting}$ of Fe–S alloys) and formational (core S content) parameters. To test the sensitivity of core radius and density/velocity structure to these parameters, crustal thickness was varied as 25–85 km, mantle potential temperature was varied as 1500–1800 K, the temperature contrast across the CMB was taken to be 0–600 K, $\Delta V_{melting}$ was taken to be 2–5%, and core S was varied as 12–21 wt%. Each combination of parameters implies a value for MOI and k_2, which can be compared to measurements of Mars-orbiting satellites (Konopliv et al., 2011; 2016) (Section 4.4).

3. Martian core formation

The composition of the Martian mantle can be used to constrain the conditions of core formation. These conditions can then be used to constrain the composition of the core.

3.1. Mantle composition and implications for the formation of Mars

An example of a Martian mantle composition produced by this model is shown in Fig. 2. To the best of our knowledge, Taylor (2013) is the only study that reports uncertainties on the Martian mantle composition (unlike, e.g., Dreibus and Wänke, 1985; Lodders and Fegley, 1997; Sanloup et al., 1999). Therefore, we use the Taylor (2013) bulk composition (refractory-enriched CI) and compare to that study's mantle assemblage. We obtain good agreement with Lodders and Fegley (1997) and Sanloup et al. (1999) when we instead use their bulk compositions. Calculated mantle abundances of major, minor, and trace elements are consistent with those of Taylor (2013), except for K (Fig. 2). Taylor (2013) treated K uniquely, obtaining its abundance from gamma ray spectroscopy measurements of the surface K/Th ratio; this methodological difference likely accounts for the discrepancy. To constrain conditions of the formation and differentiation of Mars, first the fO_2 at which primordial material equilibrated was adjusted to match the reported FeO content of the Martian mantle. The mantle FeO content implies that Mars was built of material with an initial oxidation

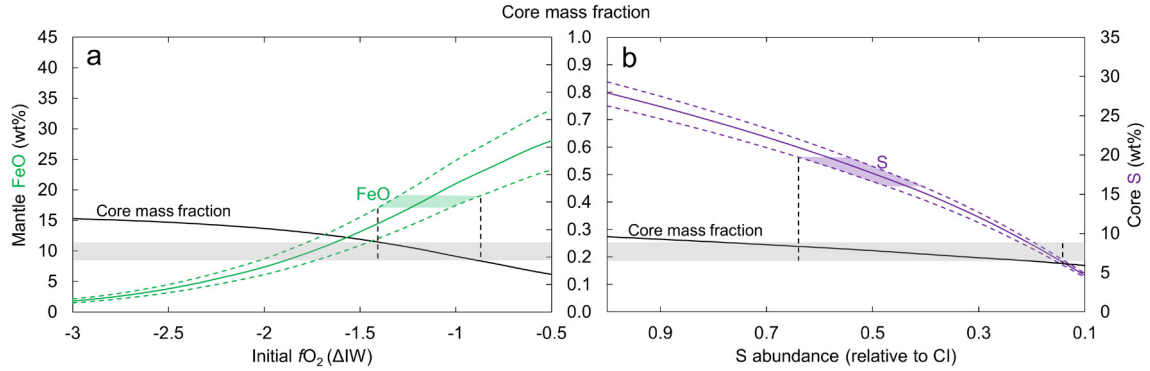

Fig. 3. a. The tradeoff between the initial fO_2 of primordial material and the partitioning of Fe between mantle and core. The green shaded region indicates the range of calculated FeO contents that are consistent with Taylor (2013), which constrain the initial fO_2 to be IW–0.9 to IW–1.4. The corresponding core mass fraction is 0.19–0.25 (horizontal shaded bar) for a bulk S content of 4.2 wt%. **b.** The tradeoff between bulk S content and S content of the core (purple). The same range in core mass fraction as in **a** (black curve and horizontal shaded bar) can be produced by varying the total S content of bulk Mars in the range 0.15–0.65 × CI for an initial oxygen fugacity of IW–1.12. The purple shaded region represents the range of core S contents from the core formation model. Dashed lines represent 95% confidence intervals. Calculation was performed for $P_{equil}/P_{CMB} = 0.55$, $k_{mantle} = 1$, and $k_{core} = 0.9$. (For interpretation of the colors in the figure(s), the reader is referred to the web version of this article.)

state of IW–1.4 to IW–0.9, which results in a final core mass fraction of 0.19–0.25 (Fig. 3a). The higher initial fO_2 and smaller core relative to Earth (e.g., Fischer et al., 2017; Rubie et al., 2011; 2015) reflects the accretion by Mars of relatively oxidized primordial material, which likely originated further from the Sun.

Constraints on the degree of equilibration were obtained by comparing the calculated mantle compositions with literature values (Fig. 4a). Possible values of k_{core} are 0.84–1.0 for whole-mantle equilibration ($k_{mantle} = 1$), based on matching the mantle abundances of TiO_2, S, and Co (within their 95% confidence intervals); other elements are consistent with this range but do not provide such tight constraints. This degree of metal equilibration is significantly higher than the k_{core} of 0.2–0.55 found for Earth (Fischer and Nimmo, 2018). Earth's lower k_{core} is consistent with the accretion of giant differentiated impactors, whose large cores may not have efficiently emulsified in the terrestrial magma ocean. A high k_{core} for Mars is consistent with the accretion of smaller bodies, possibly including undifferentiated impactors that would effectively exhibit $k_{core} \sim 1$. Varying k_{mantle} does not significantly change the mantle composition for values above ~0.4, consistent with its limited compositional effect above a certain threshold for the Earth (Fischer et al., 2017). Reducing the degree of silicate equilibration requires a corresponding increase in k_{core}.

An analogous procedure was used to constrain the depth of metal–silicate equilibration (Fig. 4b). Simultaneously matching the Martian mantle abundances of Ni, Co, and S requires that P_{equil}/P_{CMB} falls in the range 0.42–0.60 (for $k_{core} = 0.9$ and $k_{mantle} = 1$); again, other elements are consistent with this range, but do not further constrain it. This pressure range implies that, on average, equilibration took place in a deep magma ocean but shallower than the core–mantle boundary, consistent with previous arguments for a deep Martian magma ocean (e.g., Dauphas and Pourmand, 2011). A similar relative depth of equilibration was found for the Earth using comparable models (Fischer et al., 2017; Rubie et al., 2011; 2015); this may suggest a similar relative depth of melting on the two planets. This range implies an average equilibration pressure similar to the results of single-stage partitioning studies (e.g., Rai and van Westrenen, 2013; Righter and Chabot, 2011). Mars likely formed from small bodies (e.g., Kobayashi and Dauphas, 2013), but single-stage models necessarily partition elements at a fixed fO_2 and do not incorporate P–T changes as a planet grows. The more realistic model presented here includes these effects, and its agreement with the single-stage models reinforces the robustness of our results.

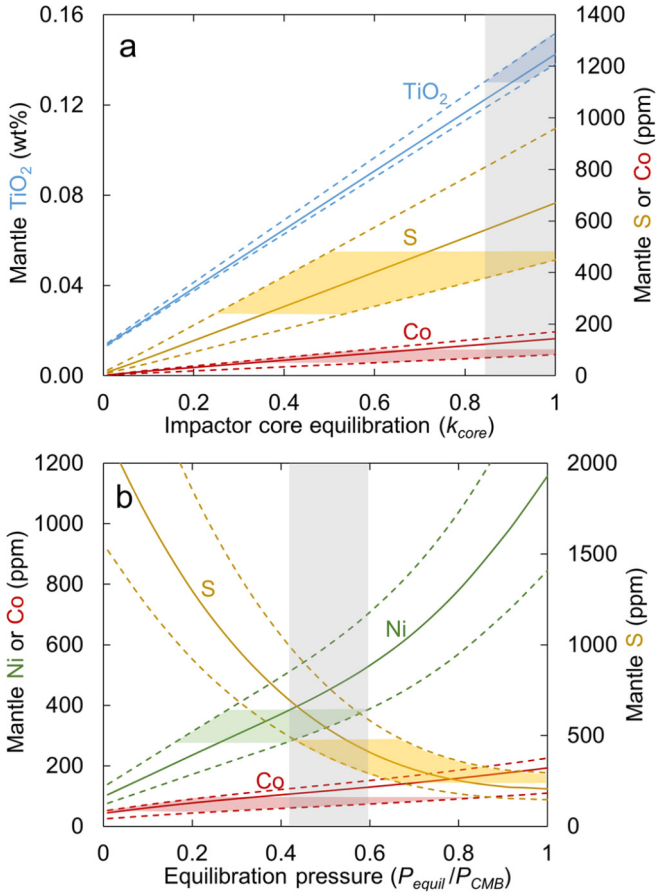

Fig. 4. a. Variations in the mantle concentrations of TiO_2 (blue), Co (red), and S (yellow) as a function of the degree of impactor core equilibration, k_{core}. Dashed lines are 95% confidence intervals. The colored regions illustrate where the calculated compositions are consistent with the previously published values of Taylor (2013) for TiO_2 and Co and Wang and Becker (2017) for S. The grey shaded bar indicates the range of k_{core} in which all three elements can be matched. These values of k_{core} suggest that most metal was emulsified and equilibrated before merging with the Martian core. Calculation was performed for whole mantle equilibration ($k_{mantle} = 1$), $P_{equil}/P_{CMB} = 0.55$, and initial fO_2 of IW–1.12. **b.** Variations in the mantle concentrations of Ni (green), Co (red), and S (yellow) as a function of core–mantle equilibration pressure (expressed as a fraction of the evolving CMB pressure). The colored regions illustrate where the calculated compositions are consistent with the previously published values of Taylor (2013) for Ni and Co and Wang and Becker (2017) for S. These pressures suggest that equilibration occurred in a deep magma ocean, but not at the core–mantle boundary. Calculation was performed for $k_{core} = 0.9$, $k_{mantle} = 1$, and initial fO_2 of IW–1.12. (For interpretation of the colors in the figure(s), the reader is referred to the web version of this article.)

3.2. Light elements in the Martian core

The core formation conditions implied by the Martian mantle composition indicate that S is the dominant light element in the core, consistent with previous studies (e.g., Lodders and Fegley, 1997; Sanloup et al., 1999; Steenstra and van Westrenen, 2018; Taylor, 2013; Dreibus and Wänke, 1985). Sulfur is siderophile at the P–T–fO_2 conditions of Martian core formation, so the majority of Martian S must be in the core. However, the mantle abundance also appears to be greater than that of the Earth (e.g., Wang and Becker, 2017), implying that bulk Mars is relatively sulfur-rich. The range of core mass fractions implied by the mantle FeO content, 0.19–0.25 (Section 3.1), can be produced by a range of volatile element depletion factors of 0.15–0.65× CI for an initial oxygen fugacity of IW–1.12 (Fig. 3b). Taylor (2013) argued for a refractory element enrichment of 1.9 × CI (equivalent to a volatile element depletion of 0.6 × CI) based on a survey of volatile lithophile element abundances. Enriching Mars in refractory elements by this factor leads to a core S content of 18–19 wt% (95% confidence interval; Supplementary Table S2). This corresponds to a mantle with 500 ppm S and a bulk Mars with 4.2 wt% S, within the bulk abundance estimates of Steenstra and van Westrenen (2018). Tuff et al. (2013) suggested a mantle with an order of magnitude more S (2500 ppm), but such a composition would require a far higher bulk S abundance than any meteorite group (>20 wt%) if the mantle S content is due to core formation. If Mars is assumed to have bulk S equivalent to an H chondrite, it would have a core S content of 12 wt%. Bulk S content equivalent to a pristine EH chondrite results in a core S content of 21 wt%; this may be taken as the upper limit for core S in a chondritic Mars since EH is the most S-rich of all chondrite groups (Lodders and Fegley, 1998).

The Martian core contains little O (<1 wt%; Supplementary Table S2) despite its oxidizing core formation conditions. This is due to the relatively modest P–T conditions of metal–silicate equilibration on Mars, since O partitions more strongly into iron alloys at higher T (e.g., Fischer et al., 2015; Ricolleau et al., 2011; Rubie et al., 2004). Steenstra and van Westrenen (2018) calculated core O content as a function of equilibration pressure in a single-stage model; at 13 GPa they found similar or slightly higher oxygen abundances compared to those found here (∼0.4–1.3 wt%). Low oxygen abundances in the Martian core agree with some previous studies (e.g., Rubie et al., 2004), though some predicted O at the few-percent level (e.g., Tsuno et al., 2011) due to an assumption of core–mantle equilibration at the modern CMB (inconsistent with our findings; Fig. 4b). The other light element considered here, Si, only enters the Martian core at trace levels (Supplementary Table S2). Like O, Si is less siderophile at lower temperatures, but it is also less siderophile at higher fO_2 (Geßmann et al., 2001; Fischer et al., 2015; Ricolleau et al., 2011), further reducing its core abundance.

C and H partitioning were not modeled despite suggestions that these may be present in the core with greater-than-trace abundances (e.g., Chi et al., 2014; Zharkov and Gudkova, 2005). There are few constraints on the planetary or mantle abundances of these highly volatile elements, and thus it is difficult to determine their total budgets. Qualitatively, Mars is too small and S-rich to dissolve substantial H in its core, with Clesi et al. (2018) estimating 60 ppm. The solubility of C is also much reduced in S-rich core alloys (Tsuno et al., 2018). For a nominal bulk C content of 1000 ppm, Tsuno et al. (2018) found that a Martian core at IW–1.0 with 16 wt% S would have ∼0.5 wt% C; this may be taken as an upper bound for the more S-rich core presented here. This estimation may be too low if Mars is C-rich; Steenstra and van Westrenen (2018) found that bulk Martian compositions with 2500–4000 ppm C can have up to 1.4 wt% C in the core. Better constraining the abundances and partitioning of these highly volatile elements is a target for future studies.

4. Geophysical properties of Mars

The compositions predicted by the core formation model were used to construct phase assemblages and produce density and velocity profiles (Figs. 5 and 6) of the Martian interior (Section 2.2). In addition to composition, these profiles depend on various geophysical properties of the Martian interior, which can be constrained by calculating each profile's mass, radius, MOI, and k_2. The resulting solution space allows for predictions of core radius and seismic properties.

4.1. The lithospheric boundary layer

Mars is a stagnant lid planet and is inferred to have a laterally variable lithosphere up to 300 km thick (e.g., Grott et al., 2013). This is a thick thermal boundary layer on a small planet, so the accompanying low-velocity zone (LVZ) may be of first-order importance for Martian seismology (Section 4.6; Fig. 6). Since the magnitude of the velocity decrease is dependent on the thermal structure of the lithosphere, mantle potential temperatures may be inferred by measuring the LVZ's seismological effects (Zheng et al., 2015).

The magnitude of this effect, however, cannot be well-constrained with our current knowledge of Martian temperature and structure. The calculations shown here use an upper mantle thermal boundary layer thickness of 200 km (Khan et al., 2018) and a range of mantle potential temperatures around 1600 K (Nimmo and Faul, 2013). Changing the mantle potential temperature at a constant lithospheric thickness requires changing the slope of the lithospheric temperature profile (Supplementary Fig. S3). Increasing potential temperature by 100 K for a 200 km lithospheric boundary decreases velocities in the LVZ by 0.2 km/s for compressional waves and 0.1 km/s for shear waves. These effects may be complicated by variations in lithospheric thickness due to the hemispherical dichotomy and the Tharsis volcanic province.

4.2. Lowermost mantle conditions

There is some disagreement as to whether the Martian mantle contains bridgmanite, the most abundant mineral of Earth's lower mantle. Some studies find that the P–T conditions of the lowermost Martian mantle lie within the bridgmanite stability field (e.g., Bertka and Fei, 1998), some do not (e.g., Khan and Connolly, 2008; Khan et al., 2018; Sohl and Spohn, 1997), and some are inconclusive (e.g., Bertka and Fei, 1997; Rivoldini et al., 2011). The experimental work of Bertka and Fei (1997) and Duncan et al. (2018) suggests that bridgmanite stability begins at ∼23 GPa in the Martian mantle. This CMB pressure corresponds to a core radius of ∼1500 km; such a core is smaller than any in Fig. 5 and is difficult to reconcile with geophysical constraints (see Section 4.4) (e.g., Khan et al., 2018). A bridgmanite layer would affect mantle convection and reduce heat flow from the core, impacting both the aerotherm and the temperature contrast across a CMB thermal boundary layer (Breuer et al., 1998; Michel and Forni, 2011). Thus, if a bridgmanite layer does exist, its thickness will strongly constrain mantle temperature (Bertka and Fei, 1997); the possibility of such a layer in the past may have influenced the Martian mantle's convective regime towards single-plume upwelling (Sohl and Spohn, 1997).

4.3. The crust

The outer layers of a planet have an outsized influence on the planet's MOI due to their large radial distance from the center

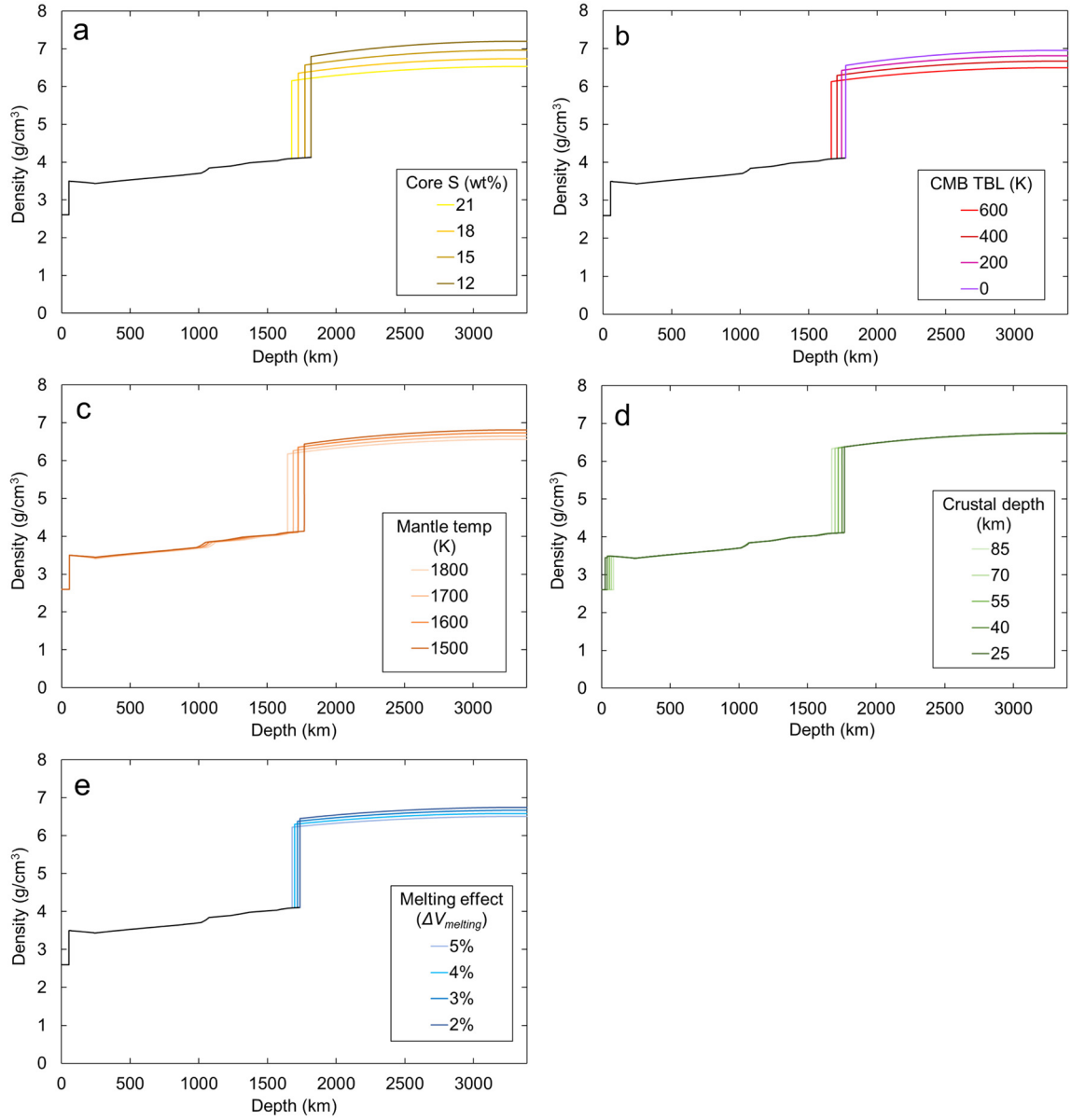

Fig. 5. Martian density profiles calculated by varying a single parameter at a time: core S content (**a**), temperature contrast between the lowermost mantle and uppermost core (assuming a thin thermal boundary layer at the CMB) (**b**), mantle potential temperature (**c**), crustal thickness (**d**), and $\Delta V_{melting}$ of Fe–S alloys (**e**). Calculations were performed for a core S content of 18 wt%, CMB TBL of 300 K, mantle potential temperature of 1600 K, crustal thickness of 55 km, and $\Delta V_{melting} = \sim 3\%$ except as noted.

of gravity. Konopliv et al. (2011) determined the Martian MOI to be 0.3644 ± 0.0005 but found that altering crustal thickness by 25 km changes the MOI by 0.0017. Some recent studies use an even tighter bound on MOI (Khan et al., 2018), but regardless of precision, uncertainties in crustal structure dominate inertia-based constraints on models of the Martian interior. Determining the average crustal properties pertinent to a spherically-symmetric model is complicated by the fact that the Martian crust contains a significant hemispheric dichotomy, various volcanic provinces, impact basins, and heterogeneous regolith. Constraints from orbital gravity measurements and surface topography imply that mean crustal thickness must lie within 57 ± 24 km (Wieczorek and Zuber, 2004). We find that within a narrow range of crustal thicknesses (55 ± 10 km), the Martian MOI can be matched with a wide range of core sizes (1500–1850 km). Fortunately, InSight measurements are likely to better constrain crustal thickness beneath the landing site (Panning et al., 2017), which will allow for tighter constraints on core size.

4.4. Core radius

We have evaluated the effects of five parameters on the core radius of Mars: the thickness of the crust, temperatures of the mantle and core, sulfur content of the core, and densities of liquid Fe–S alloys. All core radii calculated here are consistent with the core mass fraction range determined in the core formation model (Section 3.1; Fig. 3).

(1) Thickness of the crust. A thick layer of relatively light crustal material requires a larger core to maintain consistency with the Martian radius and bulk density. Varying crustal thickness in the range 25–85 km (Wieczorek and Zuber, 2004) corresponds to a change in core radius of 94 km, with thicker crusts corresponding to larger cores. The planet's MOI is very sensitive to crustal parameters, so only a small portion of this range of crustal thicknesses is consistent with measurements (Section 4.3).

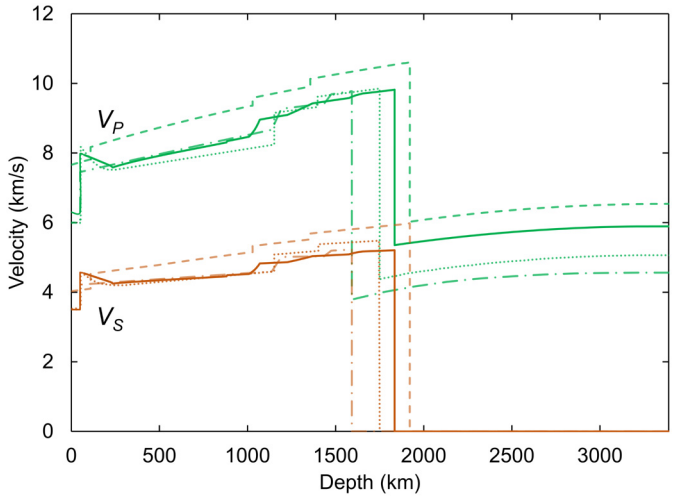

Fig. 6. Comparison of Martian compressional wave velocity (V_P, green) and shear wave velocity (V_S, brown) profiles between this study (solid lines) and several previous studies. Dashed lines: Sohl and Spohn (1997) "Model A". Dotted lines: Zheng et al. (2015) "LVZ Model". Dot-dashed lines: Zharkov and Gudkova (2005) "M14_3 Model". The profile for this study corresponds to a core sulfur content of 18 wt%, crustal thickness of 50 km, thermal boundary layer temperature contrast of 300 K, mantle potential temperature of 1600 K, and $\Delta V_{melting} = 3\%$. The low-velocity zone in the upper mantle is a consequence of the steep lithospheric temperature profile within the stagnant lid on Mars (Section 4.1).

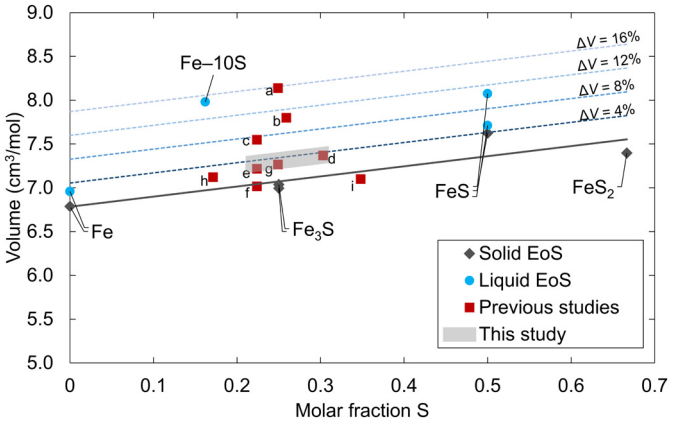

Fig. 7. Densities of solid (Chen et al., 2007; Komabayashi and Fei, 2010; Seagle et al., 2006; Thompson et al., 2016; Urakawa et al., 2004) and liquid (Anderson and Ahrens, 1994; Balog et al., 2003; Morard et al., 2018; Nishida et al., 2011) alloys in the Fe–S system calculated from equations of state at 20 GPa and 2000 K. The solid line is a linear fit to the solid data, and the dashed lines are offset from this line according to fixed $\Delta V_{melting}$ up to 16%, the 1 bar value for FeS (Kaiura and Toguri, 1979). The grey box indicates the range of S consistent with a chondritic Mars and the range of $\Delta V_{melting}$ between that of Fe and FeS at these conditions. All liquid equations of state have been extrapolated beyond the pressure conditions of the original measurements, save for the Fe–10S study (Balog et al., 2003), which was based on sink/float experiments with large (~20%) error bars. Using this data point to derive the properties of the Fe–S alloy (Khan et al., 2018; Rivoldini et al., 2011) results in an implied $\Delta V_{melting}$ greater than that of FeS, which is physically unlikely. Red squares represent some previous models of the Martian core alloy (**a**: Rivoldini et al., 2011; **b**: Khan et al., 2018; **c**: Sohl and Spohn, 1997; **d**: Zharkov and Gudkova, 2005; **e**: Kavner et al., 2001; **f**: Bertka and Fei, 1998; **g**: Sanloup et al., 1999; **h**: Lodders and Fegley, 1997; **i**: Khan and Connolly, 2008). Studies **a**–**f** are plotted at the same P–T conditions as the equation of state points, while studies **g**–**i** have fixed (P–T independent) core densities.

(2) Temperature of the mantle. Martian internal temperature profiles depend on the thermal history of the planet, its radiogenic heat production, and its convective regime. These features are not well constrained, making temperatures difficult to evaluate. Lowermost mantle temperatures of 1800–2100 K bracket the "hot" and "cold" endmembers of Rivoldini et al. (2011). This range corresponds to mantle potential temperatures of 1500–1800 K, consistent with published estimates (e.g., Nimmo and Faul, 2013). This temperature range corresponds to a change in core radius of 122 km, with larger cores corresponding to hotter mantles.

(3) CMB thermal boundary layer. Previous studies (e.g., Khan et al., 2018) have generally not considered any significant CMB temperature contrast due to the absence of a Martian geodynamo (Williams and Nimmo, 2004). It is possible that the core is hotter than the overlying mantle, leading to a thin region of rapidly increasing temperatures, as in Earth's lowermost mantle. We have investigated models with uppermost core temperatures 0–600 K above the lowermost mantle temperature, within the allowable range of CMB heat flow (see supplementary materials for more details). This range corresponds to a change in core radius of 103 km, with hotter cores being less dense and thus larger.

(4) Sulfur content of the core. Since S is lighter than Fe, an S-rich core will have a reduced alloy density, and thus must be larger. A core S content of 12–21 wt% encompasses a range of 2.0–5.4 wt% bulk Martian S, corresponding to the difference between the most S-poor (H) and S-rich (EH) chondrites (Lodders and Fegley, 1998). This range changes core radius by 141 km.

(5) Effect of melting on Fe–S alloy densities. Since the Martian core is thought to be entirely molten (Konopliv et al., 2011), its geophysical parameters must be calculated with reference to liquid Fe–S alloys. Unfortunately, there are few equation of state studies in this liquid system, and the available studies do not generally extend to the relevant P–T conditions. Using the anomalously low extrapolated densities of these extant liquid data, as some previous studies have done (e.g., Khan et al., 2018; Rivoldini et al., 2011), may lead to inaccurate interpretations of the Martian core density (Fig. 7). Several equation of state studies have pointed out that the volume change between solid and liquid Fe–S alloys should be quite small at high pressures, on the order of 1.5% for Earth's CMB (Seagle et al., 2006) and only slightly greater for Martian CMB conditions. The ambient $\Delta V_{melting}$ is ~16% for FeS (Kaiura and Toguri, 1979), dropping to only ~4–5% at a few GPa (Nishida et al., 2011). Since $\Delta V_{melting}$ of Fe is ~2% at 20 GPa (Anderson and Ahrens, 1994; Komabayashi and Fei, 2010), we have chosen to use the interpolation of the solid densities and correct for a melting effect based on $\Delta V_{melting}$ values of 2–5%, corresponding to a change in core radius of 56 km. For profiles where $\Delta V_{melting}$ was not varied, we estimated $\Delta V_{melting}$ from the eutectic melting curve of Fe–S alloys (Campbell et al., 2007), leading to a mean $\Delta V_{melting}$ of ~3% for Martian core pressures, consistent with this range.

One of the geophysical constraints on the Martian interior comes from its deformation in response to tidal forcings from the Sun, Phobos, and Deimos. The tidal Love number k_2 has been determined from spacecraft and lander tracking data, most recently in Konopliv et al. (2016), which reported a value of 0.169 ± 0.006. To evaluate the consistency between this value and our profiles, we used a simplified two-layer parameterization to calculate k_2 (see supplementary materials for more details). The dissipation of tidal energy within Mars is dependent on the rigidity and relative sizes of the core and mantle, with more rigid mantles requiring larger fluid core sizes to match k_2. Given this tradeoff, a 10% change in mean mantle rigidity would require a ~6% change in fluid core radius to match the observed k_2 value for plausible Martian core sizes. If the Martian mantle accurately reflects the volumetrically-averaged shear modulus of 73 GPa calculated here, then the core should be 1690–1870 km in radius (Supplementary Fig. S4). It is

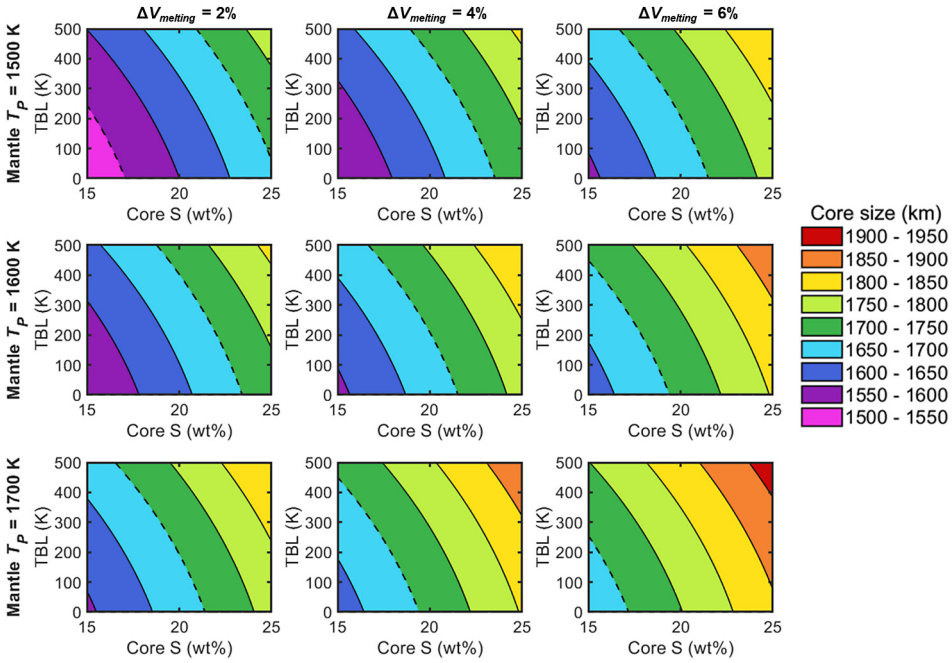

Fig. 8. Tradeoffs between parameters that influence core size as parameterized by Equation (1). Each panel represents a fixed combination of $\Delta V_{melting}$ (constant throughout each column) and mantle potential temperature (constant throughout each row) and shows the combinations of core S content and CMB thermal boundary layer temperature contrast that can produce cores of a certain size. Each contour connects cores of the same radius. All panels correspond to a 55 km crust. For this crustal thickness, the approximate MOI constraints on core size (1550–1700 km) are indicated by dashed lines. Supplementary Fig. S5 shows alternate versions of this figure corresponding to different crustal thicknesses.

possible to produce a core within this size range through various combinations of the parameters considered above, even accounting for the constraint on crustal thickness from the MOI. The relationship between core radius and the geophysical and geochemical parameters considered here is illustrated in Figs. 8 and S5, and can be parameterized by the following equation:

$$\begin{aligned} R_{core} = {} & 564(22) + 1.49(5)d_{crust} + 10.1(1.5)C^{S}_{core} \\ & + 0.183(43)\left(C^{S}_{core}\right)^2 + 0.115(10)\Delta T_{TBL} \\ & + 0.000108(8)(\Delta T_{TBL})^2 + 0.423(12)T_P \\ & + 14.8(1.1)\Delta V_{melting} + 0.337(59)(\Delta V_{melting})^2 \end{aligned} \quad (1)$$

where R_{core} is the radius of the core (km), d_{crust} is the thickness of the crust (km), C^{S}_{core} is the S content of the core (wt%), ΔT_{TBL} is the temperature contrast across the core–mantle thermal boundary layer (K), T_P is the mantle potential temperature (K), and $\Delta V_{melting}$ is the core alloy's volume change of melting (%; e.g., for a 2% volume change of melting, $\Delta V_{melting} = 2$). Numbers in parentheses represent one standard deviation on the last digits. This equation reproduces our geophysical model with a root mean squared misfit of 9 km for core radii of 1450–2000 km and the parameter ranges listed earlier in this section. It should not be applied to core sizes or parameter values outside these ranges. Future seismological constraints on crustal thickness and core radius can be inserted into this equation to help constrain geophysical properties of the Martian interior.

It is possible that the Martian mantle is less rigid than the melt-free, anhydrous, infinite-frequency idealization depicted here and in other studies. Shear moduli are lowered by the presence of water or partial melts in the mantle. Since many thousand ppm of water are needed to reduce the shear moduli of major mantle minerals by a few percent (e.g., Jacobsen et al., 2008; Wang et al., 2003), the 300 ppm water suggested to reside in the Martian mantle (Taylor, 2013) would not significantly reduce the mean shear modulus. Partial melting is another possibility; fluids cannot support shear stress, so partial melts would decrease the shear modulus of the mantle. Selecting a crust size of 55 km, potential temperature of 1600 K, core S content of 18 wt%, no TBL, and $\Delta V_{melting}$ of 3% returns a core 1620 km in radius. To match k_2, this core would require a mean mantle rigidity of 55 GPa, a 15% reduction from our nominal value, which may be obtained if there is volumetrically significant melting beneath the Martian lithosphere (Duncan et al., 2018). Ultimately, some combination of mantle-softening and core-expanding parameters must be responsible for the observed Martian k_2.

4.5. Density and velocity profiles of the Martian interior

We consider the effects of the same five geochemical and geophysical parameters (crust thickness, core and mantle T, core S content, Fe–S $\Delta V_{melting}$) on the density and velocity structure of the Martian interior (Figs. 5 and 6). Our results share much in common with previous LVZ models (Section 4.1), such as the large contrast between adiabatic and lithospheric temperatures (Nimmo and Faul, 2013) and a gradual olivine–wadsleyite phase transition due to the high FeO content. This study predicts a V_S in the lowermost mantle that is smaller than V_P at the top of the core, whereas the otherwise similar LVZ model of Zheng et al. (2015) does not (Fig. 6). The lower V_P of Zheng et al. (2015) is likely due to their use of FeS data for the thermophysical properties of the core alloy; FeS has a reduced density and bulk modulus compared to our composition.

4.6. Seismic properties

Using the Mineos software (Masters et al., 2011), mode center frequencies for the suite of models have been calculated (Fig. 9a and S6). Overall, as expected, radial, core-sensitive, and Stonely modes are affected by adjusting the five parameters described above. Stonely modes are confined to the CMB and are very challenging to observe even on Earth. Modes with center frequencies below 5 mHz are unlikely to be detectable on Mars (Panning et al.,

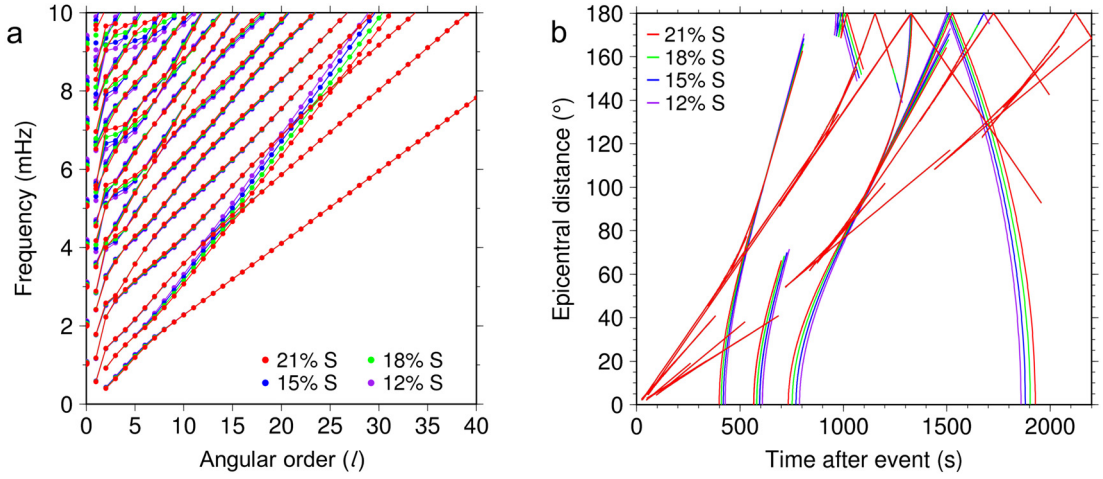

Fig. 9. Seismological observables corresponding to four models with different core S contents. **a.** Normal mode center frequencies. The radial modes sit on the vertical axis ($l = 0$). InSight's broadband seismometer is expected to be unable to detect those modes under 5 mHz. **b.** Body wave travel time predictions for a 5 km deep marsquake. Seismic phases P, PP, PcP, P_{diff}, S, SS, ScS, S_{diff}, PcS, ScP, SP, PKP, SKS, and SKKS are shown. Calculations are performed for a CMB TBL of 300 K, mantle potential temperature of 1600 K, crustal thickness of 55 km, and $\Delta V_{melting} = \sim 3\%$.

2017), but radial modes (on the left of Fig. 9a) above this period may display changes in frequency of several percent. While not affected by the physical properties of the core itself, models with different crustal thicknesses and mantle potential temperatures will result in different frequencies for the fundamental modes, which are a target for observation (Bissig et al., 2018). Thus, any observations of normal modes on Mars will aid in discrimination between these different models of Martian formation.

Body wave travel times (Fig. 9b) were calculated with the TauP toolkit (Crotwell et al., 1999), and show that a range of phases that reflect at the CMB or travel through the core are sensitive to the parameters explored here. As all the models investigated have an LVZ in the upper mantle (Section 4.1), shadow zones are evident in the travel time curves, most prominently in the direct S phase. Models with larger cores show earlier arriving core-reflected phases (e.g., ScS), whilst signals like PKP are delayed, as V_P in the core is lower than that of the mantle. SKS, which travels through the mantle as a shear wave and through the liquid core as a compressional wave, has delay times that vary little through the model suite, as V_S in the mantle is very close to V_P in the core.

The InSight site is roughly 20° from Cerberus Fossae, which has been suggested to be a site of high seismic activity (Taylor et al., 2013). At such a distance, one of the clearest core signals we hope to observe will be ScS. Fig. 10 shows predicted travel times for this phase at this epicentral distance for the full model suite. Nearly all the parameters behave in the same way: shorter ScS travel times correspond to larger core radii. Thus, even though all properties may not be discernable from such an observation, a travel time should permit us to roughly estimate core radius in this framework. Mantle potential temperature has effects on the radius–ScS time relationship that are not co-linear with the other parameters because a hotter potential temperature both decreases mantle velocities and changes core radius. Both crustal thickness and mantle potential temperature may be obtainable from other seismological observables (e.g., receiver function analysis for the former, and estimates of the sub-lithospheric LVZ for the latter), making this kind of analysis more valuable as the parameter space is narrowed down.

To use ScS travel time data, marsquakes must be relatively accurately located. The InSight mission requires that events be located within 25% of the true epicentral distance and 20% of the true back-azimuth. This level of error at an epicentral distance of 20° would change ScS arrival time by ~10 seconds, impairing the use of this kind of data even with an accurate seismic model. However, the results of the Marsquake Service blind test (Clinton et al., 2017) suggest that many Martian events may be located to a much higher degree of accuracy (van Driel et al., 2019). The utility of ScS observations in determining core radius will be determined by the degree of structural complexity, the level and distribution of seismicity on Mars, and the amount of "noise" or unwanted signal present as ScS is recorded.

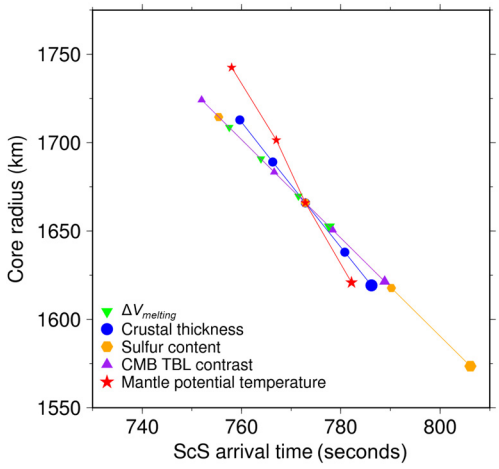

Fig. 10. Relationship between core radius and predicted ScS arrival time. Travel times are predicted for an epicentral distance of 20° and a marsquake depth of 5 km. The impact of each of the five parameters on core radius is discussed in Section 4.4. In each case the larger symbol corresponds to the lowest value of the parameter that is being varied. Calculations were performed for a core S content of 18 wt%, CMB TBL of 300 K, mantle potential temperature of 1600 K, crustal thickness of 55 km, and $\Delta V_{melting} = \sim 3\%$ except as noted.

5. Conclusions

A multi-stage core formation model successfully reproduces meteorite-based abundances of most elements in the bulk silicate Mars and has been used to determine conditions of core formation and the composition of the Martian core. The high FeO content of the Martian mantle relative to that of Earth is due to formation from primordial material initially equilibrated at an oxygen fugacity between IW–0.9 and IW–1.4. On average, >84% of incoming metal was equilibrated with >40% of the Martian mantle, and equilibration took place at a depth of 42–60% of the evolving CMB pressure. The light element composition of the Martian

core is dominated by S (18–19 wt%), with <1 wt% O and negligible Si, consistent with some previous models (e.g., Rubie et al., 2004; Steenstra and van Westrenen, 2018).

We have considered the possible ranges of various geophysical parameters (mantle and core temperatures, crustal thickness, and density of the Fe–S core alloy) and evaluated the effects of varying these parameters on the structure of the Martian interior. The core alloy densities calculated here are somewhat higher than those of previous studies due to different interpretations of the Fe–S equation of state data. Conservative parameter combinations imply that the core could be as small as 1620 km, though this size is not consistent with geophysical constraints on tidal Love number k_2 unless part of the Martian mantle is significantly softened by the presence of melt or water. Larger values of crustal thickness, mantle temperature, core temperature, or S content imply larger cores (Equation (1)). If the Martian mantle is not subject to any softening effects, the core can be as large as 1870 km while maintaining consistency with geophysical observations. We have calculated seismic phase arrival times and planetary normal modes for a variety of parameter combinations to facilitate comparison with InSight's seismological measurements. Whatever the results of these observations, the actual core radius implies a particular combination of geophysical and geochemical parameters, meaning that constraints on core radius will help elucidate the thermal, physical, and compositional state of the Martian interior.

Declaration of competing interest

The authors declare that they have no known competing financial interests or personal relationships that could have appeared to influence the work reported in this paper.

Acknowledgements

This work was supported by NASA grants NNX17AE27G and 80NSSC18K1633, National Science Foundation grants 1644399 and 1736046, and a National Science Foundation Graduate Research Fellowship (DGE1745303). We thank the editor, John Brodholt, for handling our manuscript; Bob Myhill and one anonymous reviewer for their comments on the manuscript; Yingcai Zheng and Tamara Gudkova for providing their seismic models for comparison; and Francis Nimmo, Roger Fu, and Junjie Dong for their helpful advice. This paper is InSight Contribution #110.

Appendix A. Supplementary material

Supplementary material related to this article can be found online at https://doi.org/10.1016/j.epsl.2019.115923.

References

Anderson, D.L., 1972. Internal constitution of Mars. J. Geophys. Res. 77, 789–795.
Anderson, W.W., Ahrens, T.J., 1994. An equation of state for liquid iron and implications for the Earth's core. J. Geophys. Res., Solid Earth 99, 4273–4284.
Balog, P., Secco, R., Rubie, D., Frost, D., 2003. Equation of state of liquid Fe–10 wt% S: implications for the metallic cores of planetary bodies. J. Geophys. Res., Solid Earth 108 (B2), 2142.
Bertka, C.M., Fei, Y., 1997. Mineralogy of the Martian interior up to core-mantle boundary pressures. J. Geophys. Res., Solid Earth 102, 5251–5264.
Bertka, C.M., Fei, Y., 1998. Implications of Mars Pathfinder data for the accretion history of the terrestrial planets. Science 281, 1838–1840.
Bissig, F., Khan, A., Van Driel, M., Stähler, S.C., Giardini, D., Panning, M., Drilleau, M., Lognonné, P., Gudkova, T.V., Zharkov, V.N., 2018. On the detectability and use of normal modes for determining interior structure of Mars. Space Sci. Rev. 214, 114.
Breuer, D., Yuen, D.A., Spohn, T., Zhang, S., 1998. Three dimensional models of Martian mantle convection with phase transitions. Geophys. Res. Lett. 25, 229–232.
Campbell, A.J., Seagle, C.T., Heinz, D.L., Shen, G., Prakapenka, V., 2007. Partial melting in the iron–sulfur system at high pressure: a synchrotron X-ray diffraction study. Phys. Earth Planet. Inter. 162, 119–128.
Chen, B., Gao, L., Funakoshi, K.-i., Li, J., 2007. Thermal expansion of iron-rich alloys and implications for the Earth's core. Proc. Natl. Acad. Sci. USA 104, 9162–9167.
Chi, H., Dasgupta, R., Duncan, M.S., Shimizu, N., 2014. Partitioning of carbon between Fe-rich alloy melt and silicate melt in a magma ocean – implications for the abundance and origin of volatiles in Earth, Mars, and the Moon. Geochim. Cosmochim. Acta 139, 447–471.
Clesi, V., Bouhifd, M.A., Bolfan-Casanova, N., Manthilake, G., Schiavi, F., Raepsaet, C., Bureau, H., Khodja, H., Andrault, D., 2018. Low hydrogen contents in the cores of terrestrial planets. Sci. Adv. 4, e1701876.
Clinton, J.F., Giardini, D., Lognonné, P., Banerdt, B., van Driel, M., Drilleau, M., Murdoch, N., Panning, M., Garcia, R., Mimoun, D., 2017. Preparing for InSight: an invitation to participate in a blind test for Martian seismicity. Seismol. Res. Lett. 88, 1290–1302.
Connolly, J., 2009. The geodynamic equation of state: what and how. Geochem. Geophys. Geosyst. 10, Q10014.
Crotwell, H.P., Owens, T.J., Ritsema, J., 1999. The TauP toolkit: flexible seismic travel-time and ray-path utilities. Seismol. Res. Lett. 70, 154–160.
Dauphas, N., Pourmand, A., 2011. Hf–W–Th evidence for rapid growth of Mars and its status as a planetary embryo. Nature 473, 489–492.
Dreibus, G., Wänke, H., 1985. Mars, a volatile-rich planet. Meteoritics 20, 367–381.
Duncan, M.S., Schmerr, N.C., Bertka, C.M., Fei, Y., 2018. Extending the solidus for a model iron-rich Martian mantle composition to 25 GPa. Geophys. Res. Lett. 45, 10211–10220.
Fischer, R.A., Nimmo, F., 2018. Effects of core formation on the Hf–W isotopic composition of the Earth and dating of the Moon-forming impact. Earth Planet. Sci. Lett. 499, 257–265.
Fischer, R.A., Nakajima, Y., Campbell, A.J., Frost, D.J., Harries, D., Langenhorst, F., Miyajima, N., Pollok, K., Rubie, D.C., 2015. High pressure metal–silicate partitioning of Ni, Co, V, Cr, Si, and O. Geochim. Cosmochim. Acta 167, 177–194.
Fischer, R.A., Campbell, A.J., Ciesla, F.J., 2017. Sensitivities of Earth's core and mantle compositions to accretion and differentiation processes. Earth Planet. Sci. Lett. 458, 252–262.
Geßmann, C., Wood, B., Rubie, D., Kilburn, M., 2001. Solubility of silicon in liquid metal at high pressure: implications for the composition of the Earth's core. Earth Planet. Sci. Lett. 184, 367–376.
Grott, M., Baratoux, D., Hauber, E., Sautter, V., Mustard, J., Gasnault, O., Ruff, S.W., Karato, S.-I., Debaille, V., Knapmeyer, M., 2013. Long-term evolution of the Martian crust-mantle system. Space Sci. Rev. 174, 49–111.
Helffrich, G., 2017. Mars core structure—concise review and anticipated insights from InSight. Prog. Earth Planet. Sci. 4, 24.
Jacobsen, S.D., Jiang, F., Mao, Z., Duffy, T.S., Smyth, J.R., Holl, C.M., Frost, D.J., 2008. Effects of hydration on the elastic properties of olivine. Geophys. Res. Lett. 35, L14303.
Kaiura, G.H., Toguri, J.M., 1979. Densities of the molten FeS, FeS–Cu_2S and Fe–S–O systems—utilizing a bottom-balance Archimedean technique. Can. Metall. Q. 18, 155–164.
Kavner, A., Duffy, T.S., Shen, G., 2001. Phase stability and density of FeS at high pressures and temperatures: implications for the interior structure of Mars. Earth Planet. Sci. Lett. 185, 25–33.
Khan, A., Connolly, J.A.D., 2008. Constraining the composition and thermal state of Mars from inversion of geophysical data. J. Geophys. Res., Planets 113, E07003.
Khan, A., Liebske, C., Rozel, A., Rivoldini, A., Nimmo, F., Connolly, J., Plesa, A.C., Giardini, D., 2018. A geophysical perspective on the bulk composition of Mars. J. Geophys. Res., Planets 123, 575–611.
Kobayashi, H., Dauphas, N., 2013. Small planetesimals in a massive disk formed Mars. Icarus 225, 122–130.
Komabayashi, T., Fei, Y., 2010. Internally consistent thermodynamic database for iron to the Earth's core conditions. J. Geophys. Res., Solid Earth 115, B03202.
Konopliv, A.S., Asmar, S.W., Folkner, W.M., Karatekin, Ö., Nunes, D.C., Smrekar, S.E., Yoder, C.F., Zuber, M.T., 2011. Mars high resolution gravity fields from MRO, Mars seasonal gravity, and other dynamical parameters. Icarus 211, 401–428.
Konopliv, A.S., Park, R.S., Folkner, W.M., 2016. An improved JPL Mars gravity field and orientation from Mars orbiter and lander tracking data. Icarus 274, 253–260.
Lodders, K., Fegley, B., 1997. An oxygen isotope model for the composition of Mars. Icarus 126, 373–394.
Lodders, K., Fegley, B., 1998. The Planetary Scientist's Companion. Oxford University Press.
Mare, E.R., Tomkins, A.G., Godel, B.M., 2014. Restriction of parent body heating by metal-troilite melting: thermal models for the ordinary chondrites. Meteorit. Planet. Sci. 49, 636–651.
Masters, G., Barmine, M., Kientz, S., 2011. Mineos: User Manual Version 1.0.2. California Institute of Technology, Pasadena, CA.
Michel, N., Forni, O., 2011. Mars mantle convection: influence of phase transitions with core cooling. Planet. Space Sci. 59, 741–748.
Morard, G., Bouchet, J., Rivoldini, A., Antonangeli, D., Roberge, M., Boulard, E., Denoeud, A., Mezouar, M., 2018. Liquid properties in the Fe-FeS system under moderate pressure: tool box to model small planetary cores. Am. Mineral. 103, 1770–1779.
Nimmo, F., Faul, U.H., 2013. Dissipation at tidal and seismic frequencies in a melt-free, anhydrous Mars. J. Geophys. Res., Planets 118, 2558–2569.

Nishida, K., Ohtani, E., Urakawa, S., Suzuki, A., Sakamaki, T., Terasaki, H., Katayama, Y., 2011. Density measurement of liquid FeS at high pressures using synchrotron X-ray absorption. Am. Mineral. 96, 864–868.
O'Brien, D.P., Walsh, K.J., Morbidelli, A., Raymond, S.N., Mandell, A.M., 2014. Water delivery and giant impacts in the 'Grand Tack' scenario. Icarus 239, 74–84.
Panning, M., Lognonné, P., Bruce Banerdt, W., Garcia, R., Golombek, M., Kedar, S., Knapmeyer-Endrun, B., Mocquet, A., Teanby, N., Tromp, J., Weber, R., Beucler, E., Blanchette-Guertin, J.-F., Bozdağ, E., Drilleau, M., Gudkova, T., Hempel, S., Khan, A., Lekić, V., Murdoch, N., Plesa, A.-C., Rivoldini, A., Schmerr, N., Ruan, Y., Verhoeven, O., Gao, C., Christensen, U., Clinton, J., Dehant, V., Giardini, D., Mimoun, D., Thomas Pike, W., Smrekar, S., Wieczorek, M., Knapmeyer, M., Wookey, J., 2017. Planned products of the Mars structure service for the InSight mission to Mars. Space Sci. Rev. 211, 611–650.
Plesa, A.-C., Padovan, S., Tosi, N., Breuer, D., Grott, M., Wieczorek, M.A., Spohn, T., Smrekar, S.E., Banerdt, W.B., 2018. The thermal state and interior structure of Mars. Geophys. Res. Lett. 45, 12198–12209.
Rai, N., van Westrenen, W., 2013. Core-mantle differentiation in Mars. J. Geophys. Res., Planets 118, 1195–1203.
Ricolleau, A., Fei, Y., Corgne, A., Siebert, J., Badro, J., 2011. Oxygen and silicon contents of Earth's core from high pressure metal–silicate partitioning experiments. Earth Planet. Sci. Lett. 310, 409–421.
Righter, K., Chabot, N., 2011. Moderately and slightly siderophile element constraints on the depth and extent of melting in early Mars. Meteorit. Planet. Sci. 46, 157–176.
Rivoldini, A., Van Hoolst, T., Verhoeven, O., Mocquet, A., Dehant, V., 2011. Geodesy constraints on the interior structure and composition of Mars. Icarus 213, 451–472.
Rubie, D.C., Gessmann, C.K., Frost, D.J., 2004. Partitioning of oxygen during core formation on the Earth and Mars. Nature 429, 58–61.
Rubie, D., Frost, D., Mann, U., Asahara, Y., Nimmo, F., Tsuno, K., Kegler, P., Holzheid, A., Palme, H., 2011. Heterogeneous accretion, composition and core–mantle differentiation of the Earth. Earth Planet. Sci. Lett. 301, 31–42.
Rubie, D.C., Jacobson, S.A., Morbidelli, A., O'Brien, D.P., Young, E.D., de Vries, J., Nimmo, F., Palme, H., Frost, D.J., 2015. Accretion and differentiation of the terrestrial planets with implications for the compositions of early-formed Solar System bodies and accretion of water. Icarus 248, 89–108.
Rudge, J.F., Kleine, T., Bourdon, B., 2010. Broad bounds on Earth's accretion and core formation constrained by geochemical models. Nat. Geosci. 3, 439–443.
Sanloup, C., Jambon, A., Gillet, P., 1999. A simple chondritic model of Mars. Phys. Earth Planet. Inter. 112, 43–54.
Seagle, C.T., Campbell, A.J., Heinz, D.L., Shen, G., Prakapenka, V.B., 2006. Thermal equation of state of Fe_3S and implications for sulfur in Earth's core. J. Geophys. Res., Solid Earth 111, B06209.
Sohl, F., Spohn, T., 1997. The interior structure of Mars: implications from SNC meteorites. J. Geophys. Res., Planets 102, 1613–1635.
Steenstra, E.S., van Westrenen, W., 2018. A synthesis of geochemical constraints on the inventory of light elements in the core of Mars. Icarus 315, 69–78.
Stixrude, L., Lithgow-Bertelloni, C., 2011. Thermodynamics of mantle minerals – II. Phase equilibria. Geophys. J. Int. 184, 1180–1213.
Taylor, G.J., 2013. The bulk composition of Mars. Chem. Erde 73, 401–420.
Taylor, J., Teanby, N., Wookey, J., 2013. Estimates of seismic activity in the Cerberus Fossae region of Mars. J. Geophys. Res., Planets 118, 2570–2581.
Thompson, E.C., Chidester, B.A., Fischer, R.A., Myers, G.I., Heinz, D.L., Prakapenka, V.B., Campbell, A.J., 2016. Equation of state of pyrite to 80 GPa and 2400 K. Am. Mineral. 101, 1046–1051.
Tsuno, K., Frost, D.J., Rubie, D.C., 2011. The effects of nickel and sulphur on the core–mantle partitioning of oxygen in Earth and Mars. Phys. Earth Planet. Inter. 185, 1–12.
Tsuno, K., Grewal, D.S., Dasgupta, R., 2018. Core-mantle fractionation of carbon in Earth and Mars: the effects of sulfur. Geochim. Cosmochim. Acta 238, 477–495.
Tuff, J., Wade, J., Wood, B., 2013. Volcanism on Mars controlled by early oxidation of the upper mantle. Nature 498, 342–345.
Urakawa, S., Someya, K., Terasaki, H., Katsura, T., Yokoshi, S., Funakoshi, K.-I., Utsumi, W., Katayama, Y., Sueda, Y.-I., Irifune, T., 2004. Phase relationships and equations of state for FeS at high pressures and temperatures and implications for the internal structure of Mars. Phys. Earth Planet. Inter. 143, 469–479.
van Driel, M., Ceylan, S., Clinton, J.F., Giardini, D., Alemany, H., Allam, A., Ambrois, D., Balestra, J., Banerdt, B., Becker, D., 2019. Preparing for InSight: evaluation of the blind test for Martian seismicity. Seismol. Res. Lett., 1518–1534.
Wang, Z., Becker, H., 2017. Chalcophile elements in Martian meteorites indicate low sulfur content in the Martian interior and a volatile element-depleted late veneer. Earth Planet. Sci. Lett. 463, 56–68.
Wang, J., Sinogeikin, S.V., Inoue, T., Bass, J.D., 2003. Elastic properties of hydrous ringwoodite. Am. Mineral. 88, 1608–1611.
Wänke, H., 1991. Chemistry, accretion, and evolution of Mars. Space Sci. Rev. 56, 1–8.
Wänke, H., Dreibus, G., 1988. Chemical composition and accretion history of terrestrial planets. Philos. Trans. R. Soc. Lond. A 325, 545–557.
Wieczorek, M.A., Zuber, M.T., 2004. Thickness of the Martian crust: improved constraints from geoid-to-topography ratios. J. Geophys. Res., Planets 109, E01009.
Williams, J.-P., Nimmo, F., 2004. Thermal evolution of the Martian core: implications for an early dynamo. Geology 32, 97–100.
Yang, S., Humayun, M., Righter, K., Jefferson, G., Fields, D., Irving, A.J., 2015. Siderophile and chalcophile element abundances in shergottites: implications for Martian core formation. Meteorit. Planet. Sci. 50, 691–714.
Zharkov, V., Gudkova, T., 2005. Construction of Martian interior model. Sol. Syst. Res. 39, 343–373.
Zheng, Y., Nimmo, F., Lay, T., 2015. Seismological implications of a lithospheric low seismic velocity zone in Mars. Phys. Earth Planet. Inter. 240, 132–141.